Semidiurnal Variations in the Budget of Angular Momentum in a General Circulation Model and in the Real Atmosphere

ROLAND A. MADDEN, HARALD LEJENÄS,* AND JAMES HACK

National Center for Atmospheric Research,+ Boulder, Colorado

(Manuscript received 2 April 1997, in final form 10 December 1997)

ABSTRACT

Diurnal and semidiurnal variations in the budget of atmospheric angular momentum are evident in a simulation by the NCAR Community Climate Model (CCM2). These variations depicted with 20-min time resolution (each time step) are used as guides to study similar variations determined from 6-hourly NCEP/NCAR Reanalysis data. A semidiurnal variation in relative angular momentum and in angular momentum related to solid body rotation of the atmosphere is found in the reanalysis. Although there is evidence that both frictional and gravity-wave drag torques play roles, the effects of semidiurnal variations in mountain torque, resulting from the migrating semidiurnal pressure wave, are most thoroughly documented.

1. Introduction

In a study of the axial component of the atmospheric angular momentum (M) budget in data from every time step of a simulation by the NCAR Community Climate Model (CCM2) we noticed a striking, mostly semidiurnal, variation. Here we look more closely at the diurnal and semidiurnal variations in the budget of M in both the model and in available observations of the real atmosphere.

That there are diurnal and semidiurnal variations in the M budget of the simulation is not surprising since they have been documented in the wind and pressure fields in studies of other general circulation model (GCM) output (e.g., Zwiers and Hamilton 1986), and in that of the CCM2 itself (Lieberman et al. 1994). That they exist in the real atmosphere has also been known for a long time. Some references that describe relevant, observed pressure and wind oscillations are Haurwitz and Cowley (1973), Wallace and Tadd (1974), Hsu and Hoskins (1989), Whiteman and Bian (1996), and Van den Dool et al. (1997).

It is important to document the diurnal changes in M in our quest for a fuller understanding of the atmosphere. In addition, they have important geodetic implications. Better estimates of the rotation rate of the earth, or length of day (LOD), have allowed its close connection to M changes to be clearly demonstrated [see review by Rosen (1993)]. To date, most related studies have considered variations in M and LOD on timescales of a few days or longer. Now, time series of rotation rate are becoming available with time resolution of 3 h and better (Freedman et al. 1994). Observed diurnal and semidiurnal changes in the earth's rotation rate are mostly explained by momentum exchanges with the ocean, but there may be some contribution from the atmosphere (e.g., Herring and Dong 1994; Ray et al. 1994; Chao et al. 1995). Here, we look at subdaily M changes, in both a GCM (CCM2) and in the real atmosphere, using NCEP/NCAR Reanalysis data.

In section 2 to follow, we briefly describe the simulated and observed variables that are studied. The diurnal and semidiurnal variations found in the CCM2 simulation are presented in section 3. Section 4 contains parallel findings from the real atmosphere as depicted in the NCEP/NCAR Reanalysis. Possible effects on the earth's rotation rate are explored in section 5 and a summary is found in section 6.

2. Variables

The M is considered as made up of two components (see Rosen 1993). One is omega momentum (M_Ω), which is angular momentum that a parcel of air at rest with respect to the earth would have by virtue of the rotation rate of the earth. This component is sometimes called the pressure or mass term by the earth rotation community. It is determined by

* Department of Meteorology, Stockholm University, Stockholm, Sweden.

+ The National Center for Atmospheric Research is sponsored by the National Science Foundation.

Corresponding author address: Dr. Roland A. Madden, NCAR, P.O. Box 3000, Boulder, CO 80307-3000.
E-mail: ram@ncar.ucar.edu

© 1998 American Meteorological Society

Unauthenticated | Downloaded 10/03/24 04:33 PM UTC

$$M_\Omega = \frac{\Omega a^4}{g} \int_0^{2\pi} \int_{-\pi/2}^{\pi/2} p_s \cos^3\phi \, d\phi \, d\lambda, \quad (1)$$

where a is the earth's radius, Ω is the earth's mean angular velocity, p_s the surface pressure, λ the longitude, and ϕ the latitude. The second is relative angular momentum (M_r) and is that part of the total M contributed by air motion relative to the earth. This part is often referred to as the wind or motion term. It is determined by

$$M_r = \frac{a^3}{g} \int_0^{p_s} \int_0^{2\pi} \int_{-\pi/2}^{\pi/2} u \cos^2\phi \, d\phi \, d\lambda \, dp, \quad (2)$$

where u is the zonal or west-to-east wind, and thus:

$$M = M_\Omega + M_r. \quad (3)$$

The rate of change of M is forced by pressure and stress torques (see, e.g., Wahr and 0ort 1984; Newton 1971). Pressure torques arise as a consequence of unequal pressure on the eastern and western sides of mountains and small-scale topographic features, and they are often referred to as mountain torques (T_m). Lower pressure to the east of mountains speeds up the rotation rate of the earth, shortens the LOD, and decreases M. Here T_m is estimated by

$$T_m = -a^3 \int_0^{2\pi} \int_{-\pi/2}^{\pi/2} p_s \cos^2\phi \frac{\partial H}{\partial x} \, d\phi \, d\lambda, \quad (4)$$

where H is the height of the earth's surface.

Friction torque (T_f) is a stress torque that always acts to slow down the winds, no matter what their direction, so they contribute to increasing M ($T_f > 0$) when acting on easterlies and decreasing M ($T_f < 0$) when acting on westerlies; T_f is given by

$$T_f = a^3 \int_0^{2\pi} \int_{-\pi/2}^{\pi/2} \tau_f \cos^2\phi \, d\phi \, d\lambda, \quad (5)$$

where τ_f is the east–west wind stress, which is negative for westerlies.

Early climate simulations tended to have too large values of M. It was recognized that small-scale features that were not included in the models could be the cause. In an attempt to include some of their effects, so-called gravity wave stress (τ_g) was introduced. It is a stress representing the interaction of the surface with the atmosphere caused by subgrid-scale vertically propagating gravity waves. Gravity wave torque (T_g) is given by

$$T_g = a^3 \int_0^{2\pi} \int_{-\pi/2}^{\pi/2} (\tau_{g,s} - \tau_{g,t}) \cos^2\phi \, d\phi \, d\lambda, \quad (6)$$

where $\tau_{g,s}$ is the gravity wave stress at the surface and, in our case, $\tau_{g,t}$ is the gravity wave stress at the top level of the model. Actually, (5) and (6) have similar form but τ_f at the top of the atmosphere is zero. As it turns out, $\tau_{g,t}$ is small but not necessarily zero. In a later version of the NCAR Community Climate Model, CCM3, Lejenäs et al. (1998, manuscript submitted to *J. Geophys. Res.*) showed that neglecting $\tau_{g,t}$ causes errors of 1–2 Hadleys.

a. Simulation

The simulation is the same as that studied in Lejenäs et al. (1997). The model has a horizontal spectral resolution of T42 with 18 levels in the vertical. The top level of the model is at 4.809 hPa and there is a rigid lid at 2.917 hPa. Time step intervals are 20 minutes. The model was discussed fully by Hack et al. (1993). The simulated data considered here consist of 2448 time steps or 34 model days starting at 30 December of year 2 of the 20-yr simulation. All the variables necessary to solve the above equations were available with one exception. The exception is τ_g at $p = 2.917$ hPa. That is $\tau_{g,t}$, which was not saved. As a result we use only the surface value of τ_g to estimate the gravity-wave drag torque, as opposed to the difference between the gravity wave stress at the top and bottom of the model atmosphere.

b. Observations

The observational data used here are the NCEP/NCAR Reanalysis products for the 14-yr period 1982–1995. For M_r, we worked with the zonal winds stored on a 2.5° lat × 2.5° long grid, interpolated to the same horizontal grid (T42) as that used in the simulation. The winds were at 14 levels in the vertical from 1000 to 10 hPa. We used pressure intervals in approximating the integral of (2) so that the lowest pressure was zero as opposed to the 2.917 hPa for the simulation data. Data were available at 0000, 0600, 1200, and 1800 UTC. In the case of τ_f and τ_g these four synoptic times are ''reference times,'' but because values are 6-h averages beginning at the reference time, they are more representative of conditions at 0300, 0900, 1500, and 2100 UTC respectively. Only January data were included.

Surface pressure, p_s, was taken from the reanalysis sigma level dataset and put on a T63 horizontal grid for computations of T_m and M_Ω. Similarly, reanalysis values of wind stress τ_f and gravity-wave drag stress τ_g were also put on a T63 horizontal grid.

Values of p_s and u are A-class data (Kalnay et al. 1996); τ_f and τ_g are B- and C-class data respectively (a discussion of the parameterizations of τ_f and τ_g can be found on the World Wide Web at http://sgi62.wwb.noaa.gov:8080/web2/tocold.html). A-class data are strongly influenced by observations; B-class are influenced by observations, but the model also has a strong influence; and C-class data are derived solely from the model. Accordingly, although we look at T_f and T_g, our emphasis is on analyzing T_m. It must also be remembered that even for A-class data the influence of the model increases as the availability of real data decreases. This will be especially true for 0600 and 1800 UTC

Unauthenticated | Downloaded 10/03/24 04:33 PM UTC

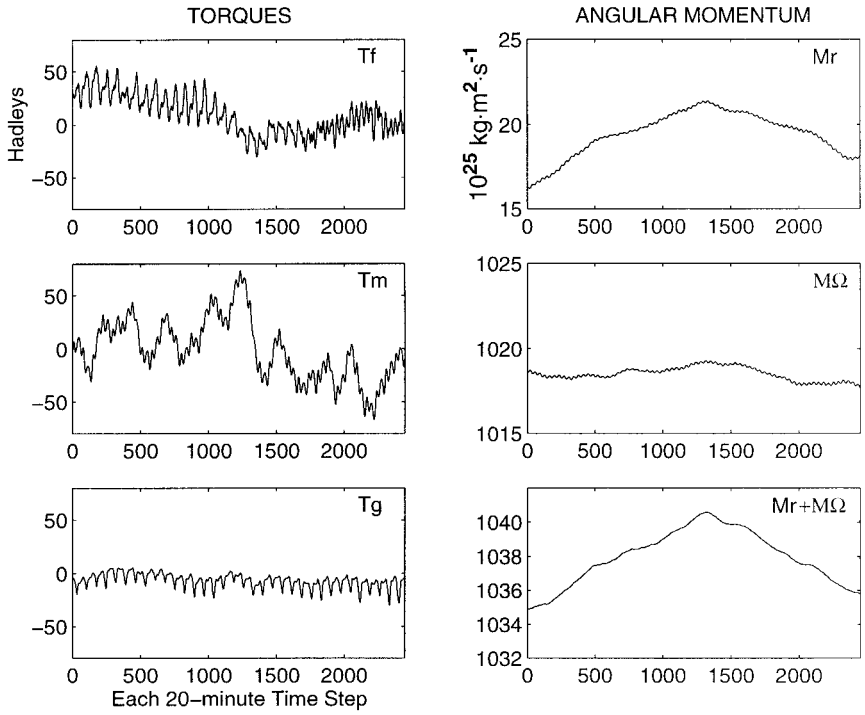

FIG. 1. Frictional (T_f), mountain (T_m), and gravity-wave drag (T_g) torques, and relative (M_r), omega (M_Ω), and total atmospheric angular momentum ($M_r + M_\Omega$) for each 20-min time step during a 34-day period from late December of a CCM2 model year through January of the next model year. Torque units are 10^{18} kg m^2 s^{-2} (Hadleys) and those of angular momentum are 10^{25} kg m^2 s^{-1}.

analyses when there are fewer rawinsondes reported than at 0000 and 1200 UTC.

3. Results from CCM2

Figure 1 shows CCM2 values of T_f, T_m, and T_g along with M_r and M_Ω for the 34-day time period extending from late December of a model year through January of the next. These data are plotted for every time step. The fast variations in T_m, M_r, and M_Ω are predominantly semidiurnal variations. Those of T_f and T_g are diurnal although there are indications of a semidiurnal variation as well.

We can isolate the diurnal and semidiurnal oscillations by averaging together the 34 values that occur at the same time step each day. The resulting averaged diurnal variations are presented in Fig. 2. Seventy-two points determine the lines in Fig. 2 and each point is the average over the 34 daily values for a given time of day. Slight changes evident from 0000 to 2400 UTC result from the average 24-h changes present in Fig. 1. The semidiurnal variation in T_m is clear. Peak-to-trough variations of the semidiurnal variation are about 15 Hadleys (1 Hadley $\equiv 10^{18}$ kg m^2 s^{-2}) as compared to variations over periods of a few days of about 50 Hadleys (from Fig. 1). The predominate diurnal variation in T_f has a range near 20 Hadleys, whereas that at longer timescales (evident in Fig. 1) is also about 50. In the case of T_g, diurnal variations are about the same size as those on the longer timescales of Fig. 1. Interestingly, phases of the large diurnal variations in T_f and in T_g are such that, taken together, they tend to reinforce the semidiurnal variations in T_m. Asterisks in Fig. 2 are observed values based on NCEP/NCAR Reanalysis data, and they will be discussed in section 4. All values in Fig. 2 are anomalies from 2448 time step averages, or in the case of the NCEP/NCAR Reanalysis data, January averages. Both averages are shown in Table 1.

The diurnal variation in the balance between the rate of change of total atmospheric angular momentum and total torque is shown in Fig. 3. The total torque is $T_f + T_m + T_g$. Values in Fig. 3 are not anomalies so that the average over 24 hours (72 time steps) need not be zero. That is, the torques can change the angular momentum during this model January. Of course, the average rate of change of M should equal the average total torque though. The slight bias, 3.2 versus 1.4 Hadleys is due, we think, to the way we estimated T_g (i.e., neglecting τ_g at the top of the model atmosphere). It is relatively small since it would take 1850 days for a negative one Hadley to reduce the average observed M_r (16×10^{25} kg m^2 s^{-1}) to zero. There is a well-marked semidiurnal variation in torque and in the resulting rate of change in M. There are maxima near 0200 and 1500

Unauthenticated | Downloaded 10/03/24 04:33 PM UTC

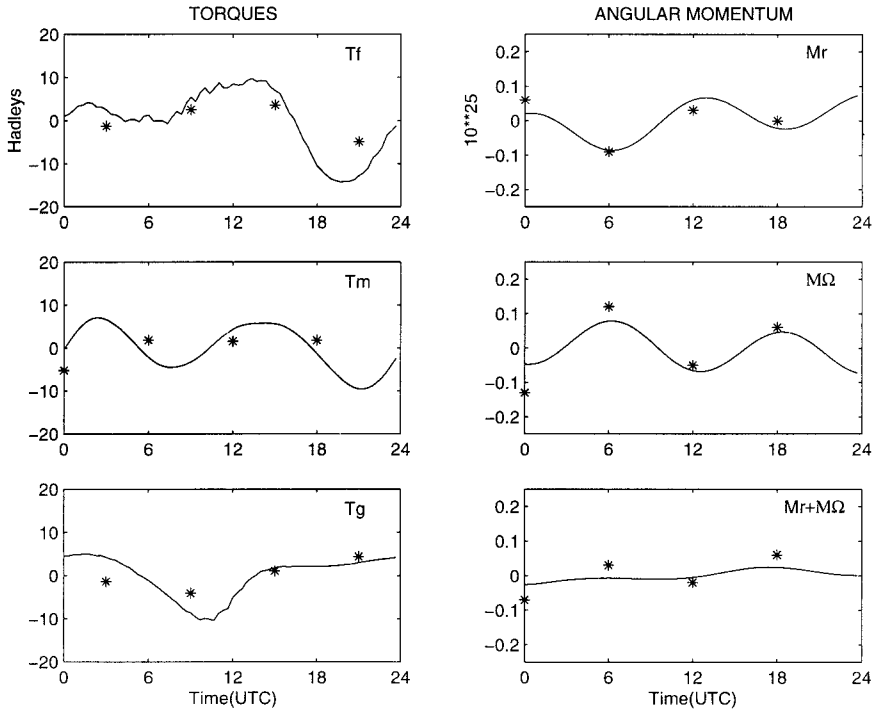

FIG. 2. As in Fig. 1 but with data composited according to the time of day showing the diurnal variations. Results from the CCM2 are depicted by the smooth line, which is determined by 72 time steps averaged over the 34 days. Asterisks denote observed values calculated from NCEP/NCAR Reanalysis data for 14 Januarys at the synoptic times of 0000, 0600, 1200, and 1800 UTC. Values for T_f and T_g are plotted three hours later because they are 6-h averages beginning at the synoptic time. All values are anomalies with the daily average subtracted.

UTC. The sum, $T_f + T_g$, and T_m contribute about equally to the semidiurnal variation in torques. In the following subsection we examine the role of T_f, T_m, and T_g separately.

a. Friction torque

Figure 4 shows the contribution of various sectors of the globe to T_f. The sum of four traces gives the total T_f of Fig. 2. The Western Hemisphere is the chief contributor to the minimum in T_f that occurs about 2100 UTC. There is also a relatively large maximum in the northern half of the Western Hemisphere shortly after 1200 UTC.

Figure 5 presents the anomalies in zonally averaged wind stress at time steps equivalent to times of 0000, 0600, 1200, and 1800 UTC for the model. Anomalies approximately cancel each other between 0000 UTC and 0600 UTC, and, accordingly, there is little difference in T_f between those two hours. There are large differences from about 20°S to 30°N between zonally averaged τ_f at 1200 and 1800 UTC.

Figure 6 presents the cumulative sum, starting at the date line, of anomaly T_f values in the 20.9°S–29.3°N

TABLE 1. The 2448 time step average of the torques in Hadleys and relative and omega momentum (10^{25} kg m^2 s^{-1}) for the CCM2 simulation and that for 14 Januarys for the NCEP/NCAR Reanalysis.

	T_f	T_m	T_g	M_r	M_Ω
CCM2	9.6	−1.1	−7.1	19.4	1018.6
NCEP/NCAR	4.6	3.7	−16.4	16.1	1018.7

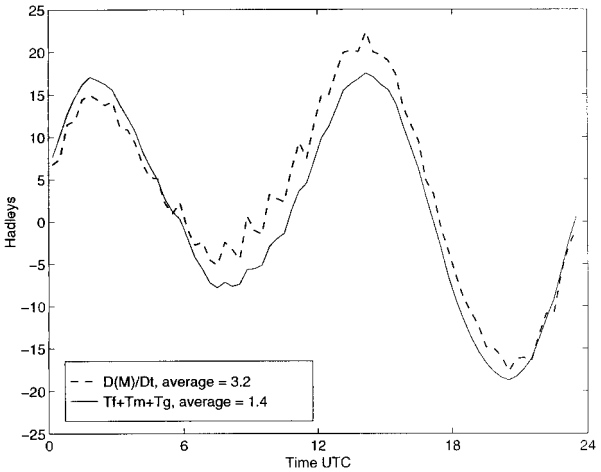

FIG. 3. The rate of change of total atmospheric angular momentum for CCM2 determined from the sum of $M_r + M_\Omega$ from Fig. 2 (dashed) and the sum of the three torques (solid) for 72 time steps (one day from 0000 to 2340 UTC). Values are not anomalies.

Unauthenticated | Downloaded 10/03/24 04:33 PM UTC

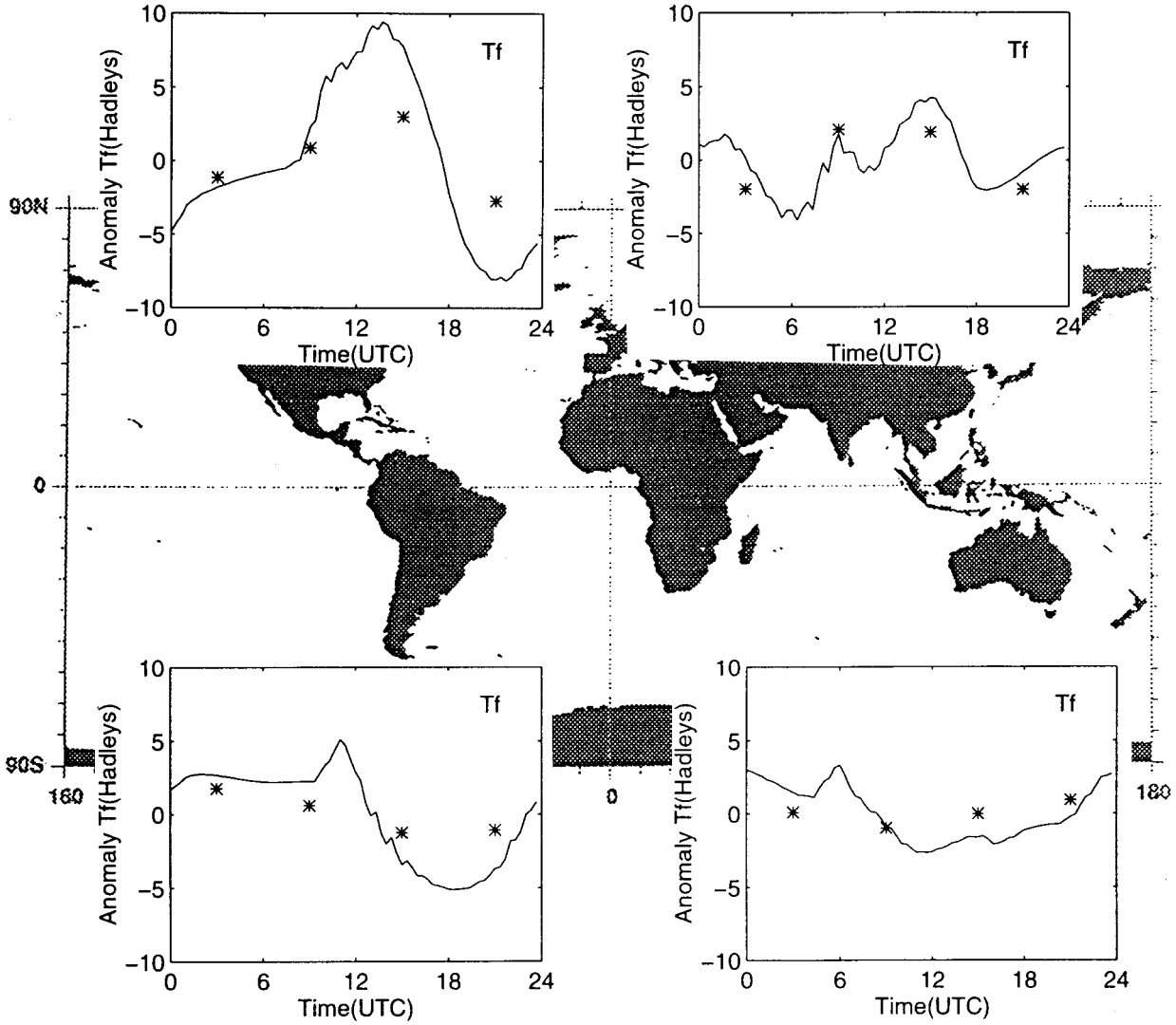

FIG. 4. Average areal contributions to anomaly T_f for 72 time steps (one day from 0000 to 2340 UTC) for CCM2 data. Asterisks denoting observed T_f are plotted at 0300, 0900, 1500, and 2100 UTC because they represent 6-h averages beginning at the four synoptic times.

latitude band. Values at 1200 and 1800 UTC begin to diverge from one another most dramatically at the longitude of North Africa. The 1200 UTC anomalies become strongly positive there and those at 1800 UTC negative. The band is dominated by easterly winds and positive average torques (not shown). A positive anomaly beginning at the African coast at 1200 UTC is consistent with stronger easterlies at the surface, possibly resulting from less vertical stability at noon and early afternoon local time. The downward sloping lines across Africa, at 1800 and 0000 UTC, represent negative anomaly contributions to T_f and indicate weaker easterlies, possibly as a result of stronger stability during the late afternoon and night there. All four of the lines in Fig. 6 level out east of Africa's east coast because there is little diurnal variability in τ_f, and therefore small anomaly contributions to T_f there.

The global change in T_f from 1200 to 1800 UTC is about 20 Hadleys (Fig. 2). That in the 20°S–30°N latitude band is also 20 Hadleys. It is not surprising that diurnal changes in τ_f in that band and, it turns out, primarily over Africa, contribute so much to the diurnal change in T_f, since the continent is near the equator and stresses there have a long moment arm. We do not know why contributions to semidiurnal changes from the Americas are small unless they reflect the smaller size of the land area.

b. Mountain torque

The semidiurnal variation in T_m (Fig. 7) is clear in the Eastern Hemisphere, although it is roughly one-quarter of a cycle out of phase between the north and south. On the other hand, north of the equator, the semi-

Unauthenticated | Downloaded 10/03/24 04:33 PM UTC

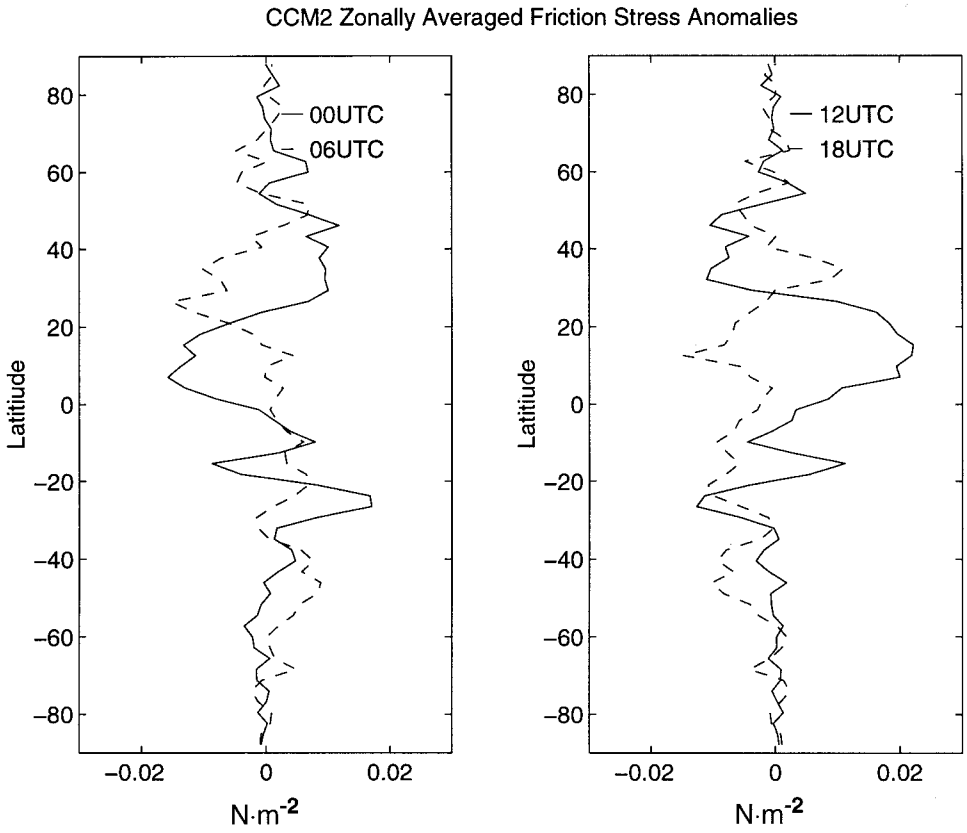

FIG. 5. Zonally average τ_f anomalies from the CCM2 for time steps near the four synoptic times of 0000 (solid), 0600 (dashed), 1200 (solid), and 1800 UTC (dashed).

diurnal variation in the Western Hemisphere is very nearly in phase with that in the Eastern Hemisphere. These semidiurnal variations are driven by a semidiurnal surface pressure tide, whose zonal scale is wavenumber two. Lieberman et al. (1994) studied the atmospheric tides in CCM2, and the semidiurnal pressure tide looks very much like the one observed in the real atmosphere [Haurwitz (1956), also reproduced in Chapman and Lindzen (1970)]. That the Rockies and Himalayas are approximately separated by 180° longitude results in the nearly in-phase variation in T_m in the two hemispheres. In section 4b we will look more closely at how the semidiurnal pressure tide results in a semidiurnal oscillation in T_m.

c. Gravity wave torque

Figure 8 shows that the diurnal variation in T_g results almost entirely from the northeast quadrant. The daily mean value of T_g for this region is −6.7 Hadleys, which, coupled with the anomalies of Fig. 8, means that T_g is negative throughout the day. The minimum anomaly value, −10 Hadleys, occurs at 9.7 h UTC. We plotted maps for the anomaly gravity wave drag stress for 0000, 0600, 1200, and 1800 UTC as well as for 9.7 h UTC, when the minimum occurs. The map for 9.7 h UTC is shown in Fig. 9. This map as well as the others (not shown here) reveals that the major contribution to the negative T_g values comes from the Himalayas and the Caucasus Mountains throughout the day. Another interesting feature is that the contribution is more negative during daytime and less negative during nighttime.

The data we extracted from the CCM2 run are not sufficient to find out what causes this variation. We speculate that there are two major reasons for the behavior of T_g. One is that the surface roughness values are highest over the Himalayas and the Caucasus Mountains. McFarlane (1987) presented a map (his Fig. 3) of the smoothed subgrid-scale orographic standard deviation used in the Canadian Climate Centre model, and the highest values are found over these two mountain massifs. Corresponding values in CCM2 are not the same; however, they do not differ much.

These surface roughness values explain the geographical distribution of the contribution to T_g. They do not, however, explain the diurnal variation. Since the parameterization of the gravity-wave drag stress torque is dependent on stability, that is, the local Brunt–Väisälä frequency (cf., Hack et al. 1993), it is likely that diabatic heating causes the observed daily variation in T_g (absorption of solar radiation during the day and/or cooling by infrared emission at night).

Unauthenticated | Downloaded 10/03/24 04:33 PM UTC

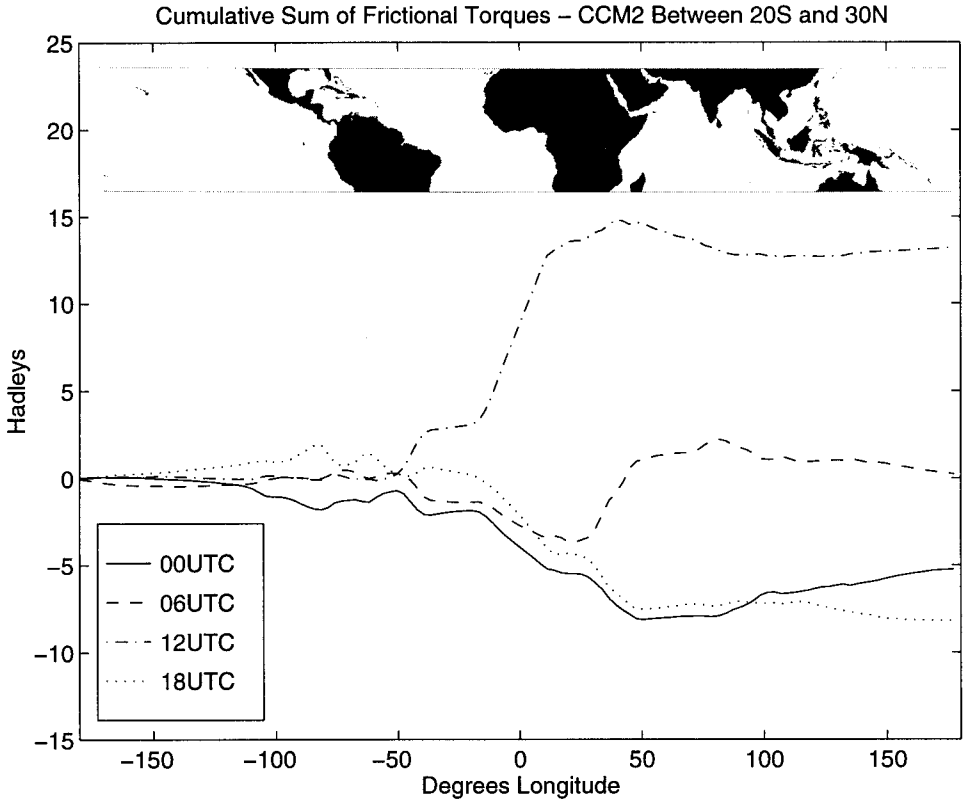

FIG. 6. Cumulative sum, starting from the date line, of anomaly frictional torques between 20.9°S and 29.3°N based on the CCM2 output for time steps near the four synoptic times of 0000, 0600, 1200, and 1800 UTC.

The parameterization of the gravity-wave drag stress also includes surface zonal winds. Thus, a third reason for the diurnal variation in T_g might be due to diurnal variations in surface winds. Unfortunately, we were not able to verify this because we did not extract surface winds from the run. We are currently beginning a similar investigation of a CCM3 simulation and expect to be able to identify what variables are most important in this interesting diurnal variation.

4. Results from NCEP/NCAR Reanalyses

The asterisks in Figs. 2, 4, 7, and 8 are determined from the 14 Januarys of the NCEP/NCAR Reanalysis. Each asterisk is the anomaly for a synoptic time from the average of all four synoptic times. The latter average is shown in Table 1. The imbalance of -8.1 Hadleys evident in Table 1 suggests a drop in M of 2.2×10^{25} kg m^2 s^{-1} during the 31 days of January. Although there is considerable year-to-year variability a drop of this magnitude during January is not uncommon (see Rosen and Salstein 1983). Agreement between anomalies based on model data and those on the reanalysis data is reasonably good. For example, the semidiurnal variation is clear in M_r and M_Ω in both datasets (Fig. 2). On the other hand, with only four points available from the reanalysis data, comparisons can be ambiguous: compare T_m values for example.

a. Friction torque

Figure 10 shows that there are relatively large diurnal variations in the zonally averaged wind stress from about 30°N to the equator, from the equator to 30°S, and in the band 60°–80°S. The northernmost band has relative maxima at 0600 and 1200 UTC (reference times), while the two in the Southern Hemisphere have their maxima at 0000 and 0600 UTC. Variations in the northern band are qualitatively similar in the simulation (Fig. 5), but those in the south are not.

Figure 11 shows the cumulative sum of anomaly frictional torques averaged between 0.9°N and 30.8°N for each of the four reference times. It is clear that the largest changes in T_f from this band occur over North Africa with relative maxima at 0600 and 1200 UTC or during the daytime hours. This result is qualitatively the same as that of the 20°S–30°N band in the simulation (Fig. 6). Actually, since τ_f is a 6-h average beginning at the reference time, values in Figs. 10 and 11 are more representative of three hours after their reference time.

Similar plots from the 0.9°S to 30.8°S band (not shown) show that changes occur near 60°W (South

Unauthenticated | Downloaded 10/03/24 04:33 PM UTC

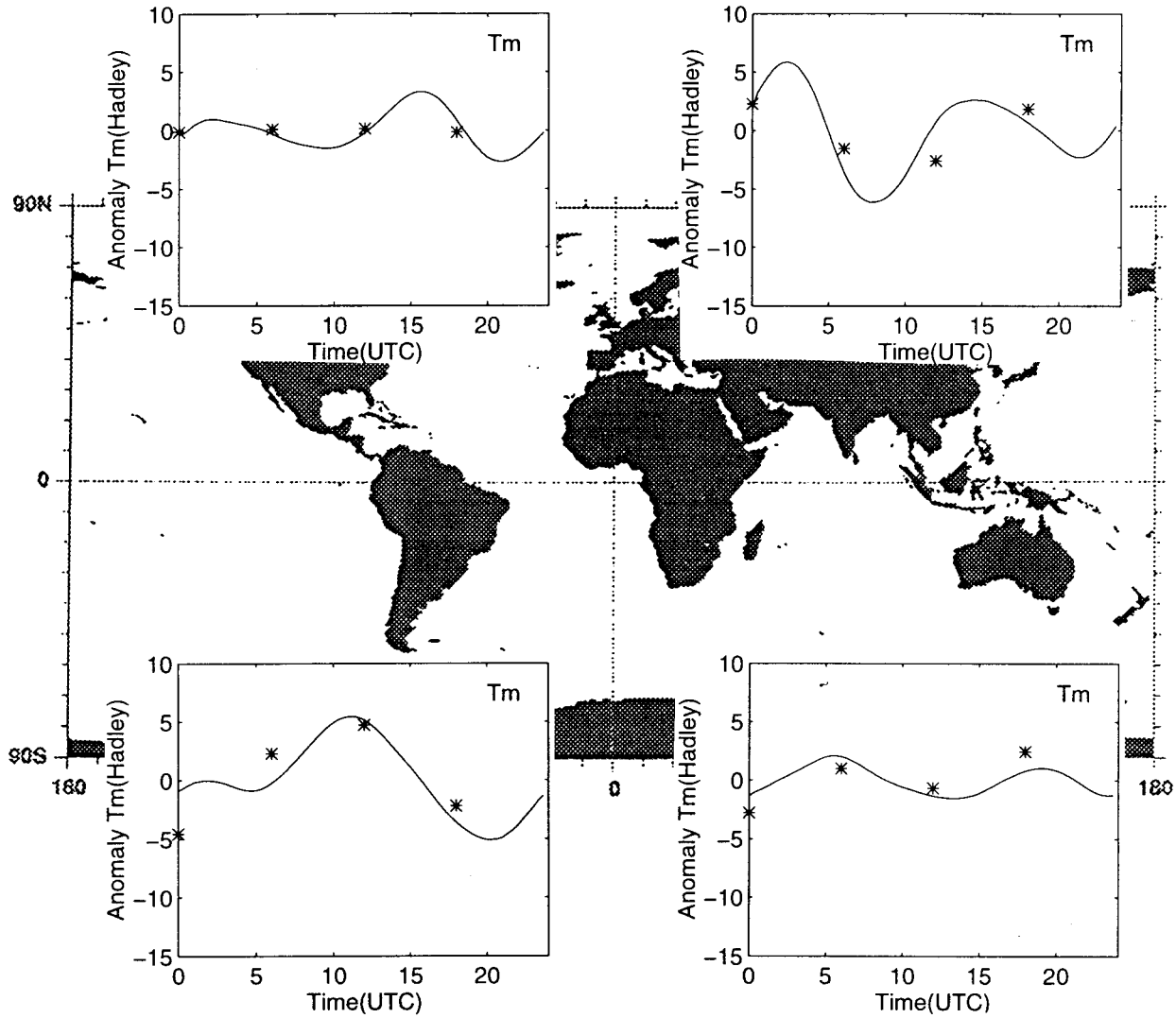

FIG. 7. Average areal contributions to anomaly T_m for 72 time steps (one day from 0000 to 2340 UTC) for CCM2 data. Asterisks denote observed values at the four synoptic times.

America), 30°E (South Africa), and 120°E (Australia). Relative maxima occur at 0000 UTC and 1800 UTC, just out of phase with the 0.9°N–30.8°N band. The changes from maxima to minima are less than 3 Hadleys in the southern band. At least in part because of the short moment arm, changes in T_f of the 60°–80°S band are less than 0.5 Hadleys. The biggest contributor to changes here (not shown) are the longitudes where a considerable part of the Antarctica landmass extends into the band (about 20°W–160°E).

From Fig. 2, the reanalysis anomaly values of $T_f = -1.3$, 2.6, 3.6, and -4.9 Hadleys occur at reference times of 0000, 0600, 1200, and 1800 UTC respectively. Corresponding values from the 0°–30°N band are -3.3, 3.8, 3.8, and -4.3 (Fig. 11). Although time and geographic variations in contributions to T_f are complex, we conclude that a large part of the diurnal variation in the global T_f from the reanalyses are accounted for by those over North Africa with minimum values during nighttime hours (time of relatively weak surface easterlies) and maximum ones during daylight hours (time of relatively strong surface easterlies). This is not unlike the results from the model data.

b. Mountain torques

The four observation times fall near the inflection points of the semidiurnal variation in T_m that is suggested by the model (Fig. 2). Accordingly T_m values determined from the reanalysis data do not exhibit a semidiurnal variation. We can attempt to learn a little more about the approximate behavior of T_m at more than the four synoptic times. We could, for example, take the amplitude of the semidiurnal pressure wave from Haur-

Unauthenticated | Downloaded 10/03/24 04:33 PM UTC

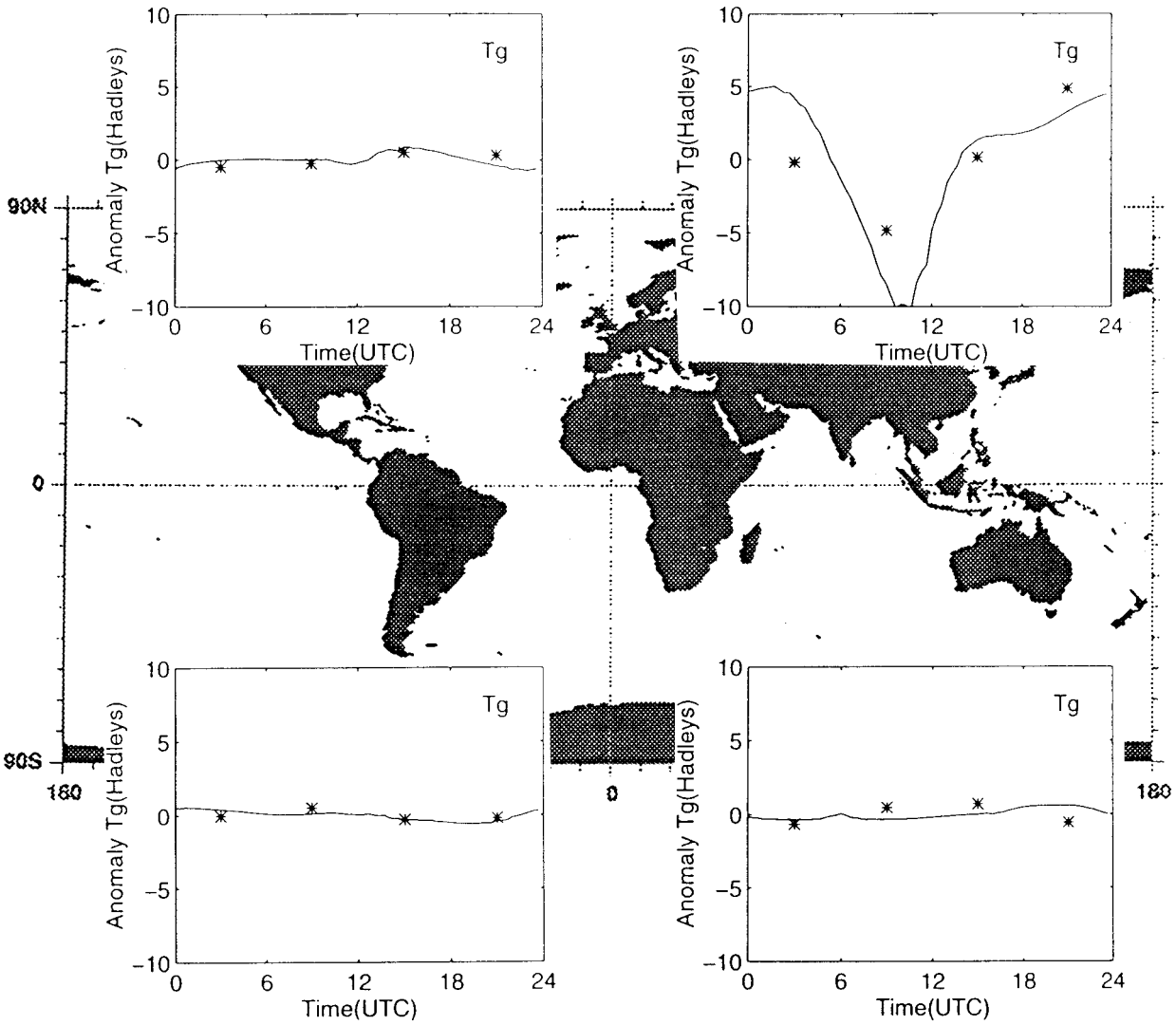

FIG. 8. Same as Fig. 4 but for T_g.

witz (1956) and simulate its passage around the world in 24 hours and compute T_m at any time resolution we like. Rather than that, we use the semidiurnal pressure wave determined from the reanalysis data. Figure 12 is the anomaly surface pressure at the four synoptic times. The wave-2 pattern is evident, as is a relative maximum in amplitude in the Tropics as shown by Haurwitz (1956). There are also some small-scale features, as, for example, near the Andes Mountains. The panels at the right of Fig. 12 show positive (negative) anomalies in zonal-mean pressure at 0600 (0000) and 1800 (1200) UTC in the Tropics, consistent with the positive (negative) anomalies in M_Ω at those times. That is, when relatively more atmospheric mass, or higher surface pressure, is near the equator, M_Ω is larger. These zonally averaged pressure changes may be related to the standing semidiurnal tidal oscillation (Haurwitz 1956; Chapman and Lindzen 1970). Changes in pressure may reflect either horizontal exchange of dry air or local changes in the amount of water vapor.

The observed semidiurnal variation in T_m was approximated at 96 time steps during a 24-h period (22.5-min intervals) by shifting separately each of the four anomaly pressure patterns of Fig. 12 two grid points westward at a time and computing T_m. Ninety-six time steps result because two grid points are a little more than 3.7° of longitude apart in our T63 data. Of course the small-scale features that may be regularly associated with the semidiurnal pressure wave, such as those near the Andes at 0000 UTC, are definitely not realistic when they are shifted over the ocean. Fortunately these features have small spatial scale, and the resulting semidiurnal variations in T_m (Fig. 13) are consistent with the semidiurnal variation suggested by the model data. There are four values plotted for each simulated time step in Fig. 13, which are based on the four separate

Unauthenticated | Downloaded 10/03/24 04:33 PM UTC

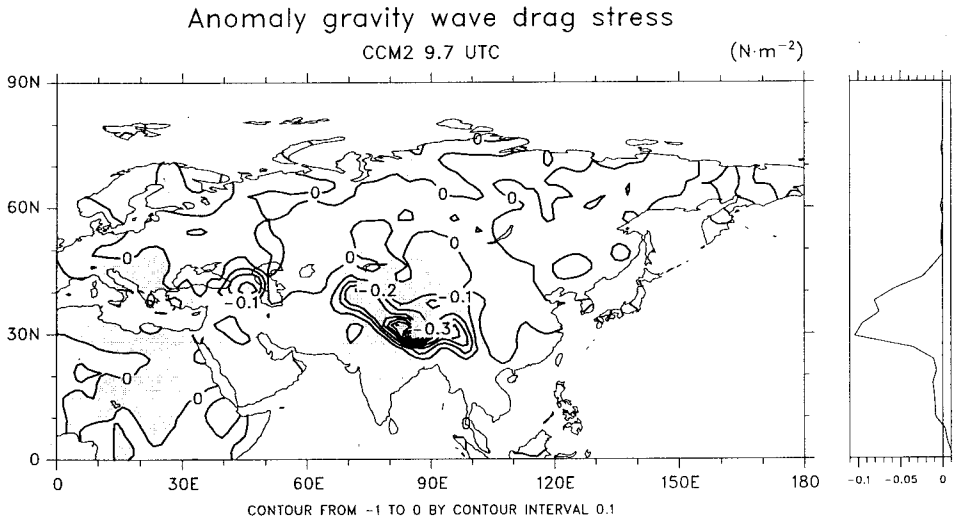

FIG. 9. Anomaly gravity wave stress (N m^{-2}) at the simulated time of 9.7 h UTC (late afternoon local time near 90°E). Shaded areas are negative. Right-hand side shows the zonal average of this stress.

pressure patterns for the synoptic times given in Fig. 12. We considered each of the patterns in Fig. 12 to be an estimate of the semidiurnal pressure wave. Therefore the spread of the four points gives a measure of uncertainty because of the uncertainty in the exact form of the semidiurnal pressure wave. This analysis points to semidiurnal changes in T_m exceeding 10 Hadleys.

Figure 14 is like Fig. 7 with areal contributions to T_m determined from the CCM2 data, and here, for clarity only, the *average* of those determined from the 0000,

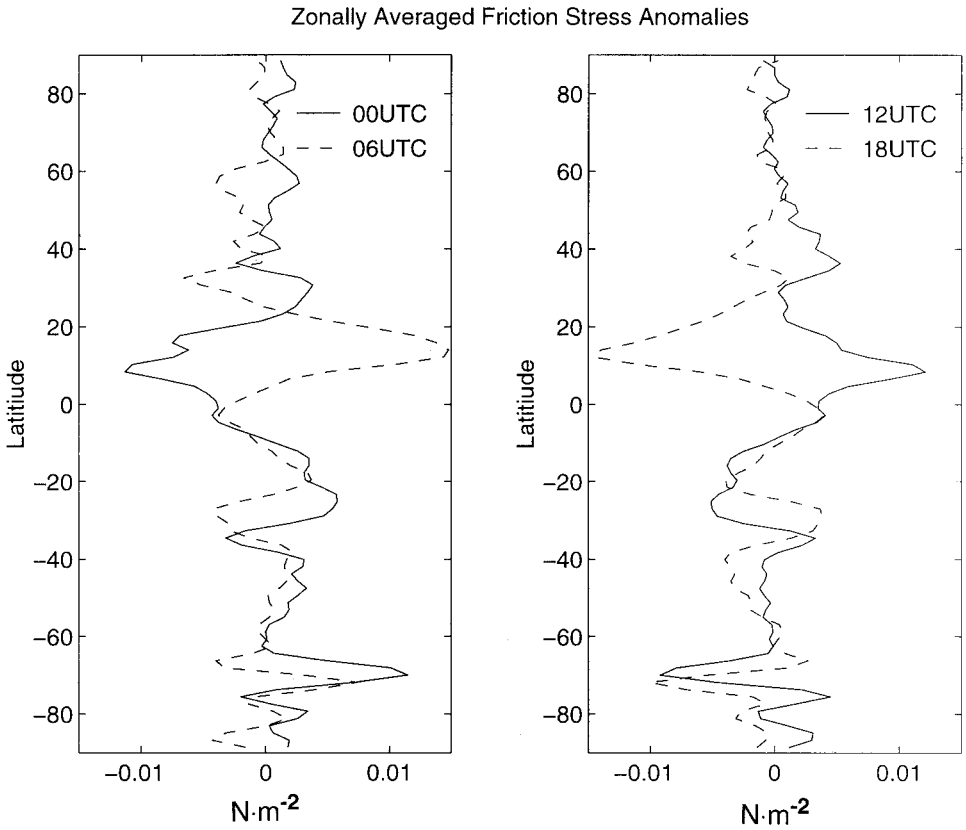

FIG. 10. As in Fig. 5 but for observed data from the NCEP/NCAR Reanalysis. Values are 6-h averages beginning at the indicated synoptic time.

Unauthenticated | Downloaded 10/03/24 04:33 PM UTC

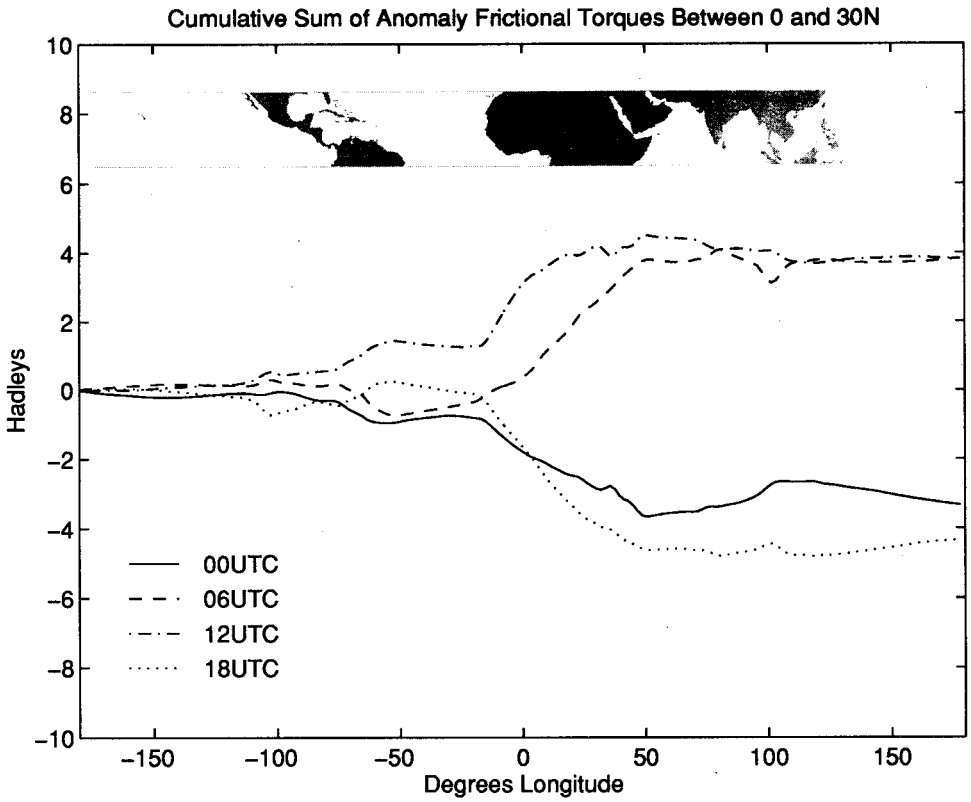

FIG. 11. Like Fig. 6 but for observed data from the NCEP/NCAR Reanalysis and for the latitude band between 0.9°N and 30.8°N. Values are base on 6-h averages beginning at the indicated synoptic time.

0600, 1200, and 1800 UTC anomaly pressure patterns of Fig. 12 are plotted. The agreement between CCM2 and observed values is very good. These four areal contributions can be directly related to mountain ranges and to the pressure anomalies of Fig. 12. For example, the lower left panel (Andes Mountains) indicates a maximum in T_m about 1200 UTC. From Fig. 12 we see that the anomaly pressure gradient is directed eastward over the Andes as it should to contribute to a positive anomaly in T_m.

c. Gravity wave torque

From Fig. 2, we see evidence for a diurnal variation in the observed T_g, but with only four points it is not possible to determine how close its phasing is to that suggested by the model data. The asterisks in Fig. 8 suggest that the biggest contribution to diurnal variation is from the northeast quadrant just as it is in the model. Similarly, a map of observed anomalies in gravity wave stress at reference time 0600 UTC (not shown) agrees well with that shown in Fig. 9 for the model data. That is, nearly all the negative anomalies occur over the Himalayas with a secondary minimum south of the Caspian Sea (as opposed to west of the Caspian Sea in Fig. 9).

We cannot diagnose the diurnal variations in T_g further. We speculate that their causes are decreased stability and possibly increased westerlies over the mountains during daylight hours. Both of these factors would contribute to increased gravity wave drag.

5. Effects on the earth's rotation rate

In the case in which changes ΔM are accompanied by an exchange of momentum solely with the solid earth we can determine resulting changes in the earth's rotation rate. If ΔM were to last at least 24 h then

$$\Delta\text{LOD} = 1.68 \times 10^{-23}\,\Delta M, \tag{7}$$

with ΔM in units of kg m^2 s^{-1} and ΔLOD, in μs (Rosen and Salstein 1983). Figure 15 shows the diurnal variation in M and, for comparison, an indication of the ΔM that would result in change of 10 μs in LOD. The M in Fig. 15 differs from that in Fig. 2 (lower right panel) because the earth undergoes elastic yielding under atmospheric pressure loading (Munk and MacDonald 1960; Barnes et al. 1983). It is an ''effective'' M (e.g., Gross 1993) given by

$$M_{\text{eff}} = 0.756M_{\Omega} + M_r. \tag{8}$$

We see that peak-to-trough semidiurnal changes are equivalent to just less than 10 μ change in LOD. We also note that using M_{eff} has resulted in model and

Unauthenticated | Downloaded 10/03/24 04:33 PM UTC

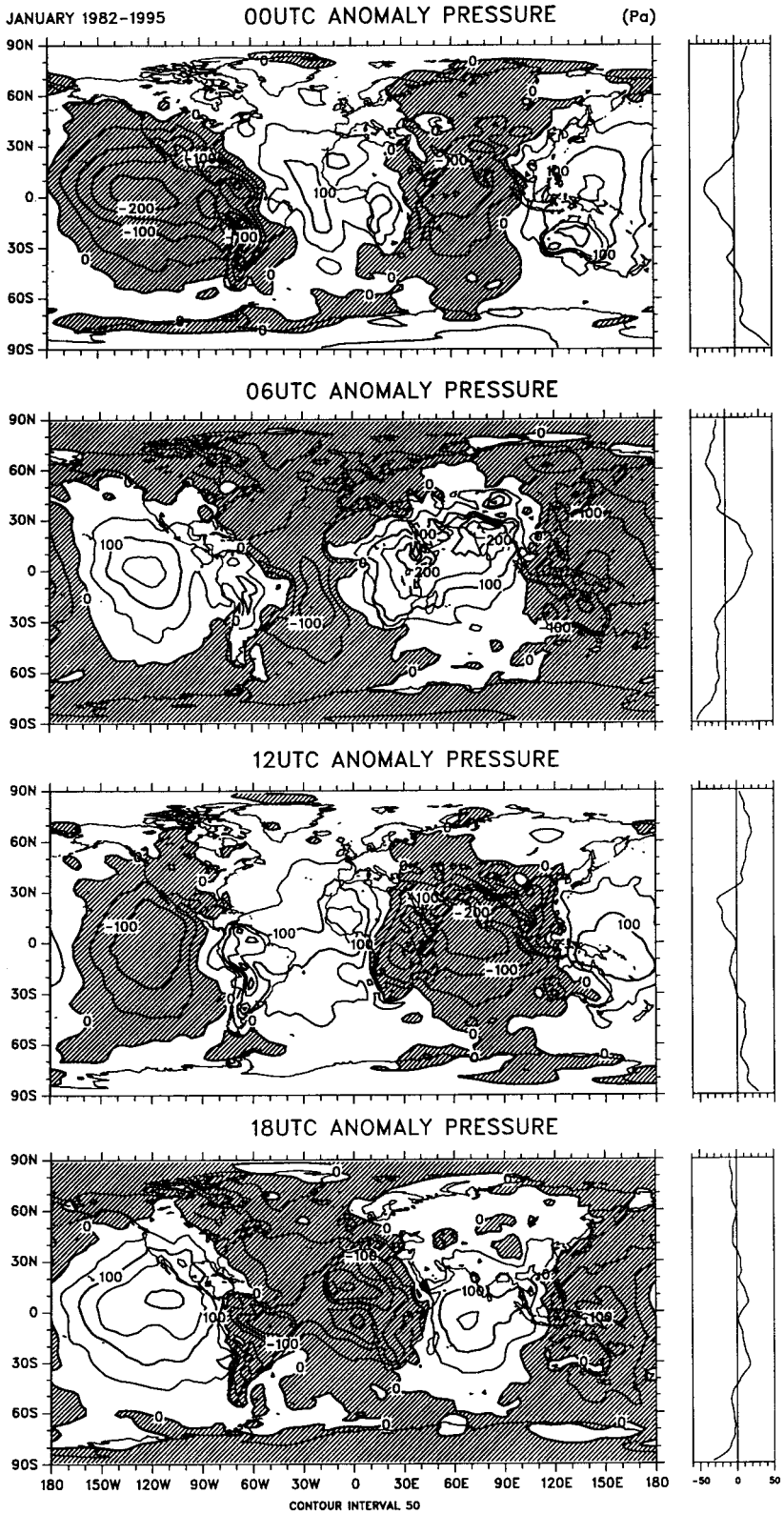

FIG. 12. Observed surface pressure anomalies at the four synoptic times determined from averages over 14 Januarys of NCEP/NCAR Reanalysis data. The anomalies are contoured in pascals (100 pascal = 1 mb). Shaded areas are negative. Panels on the right contain zonal averages of the anomalies.

Unauthenticated | Downloaded 10/03/24 04:33 PM UTC

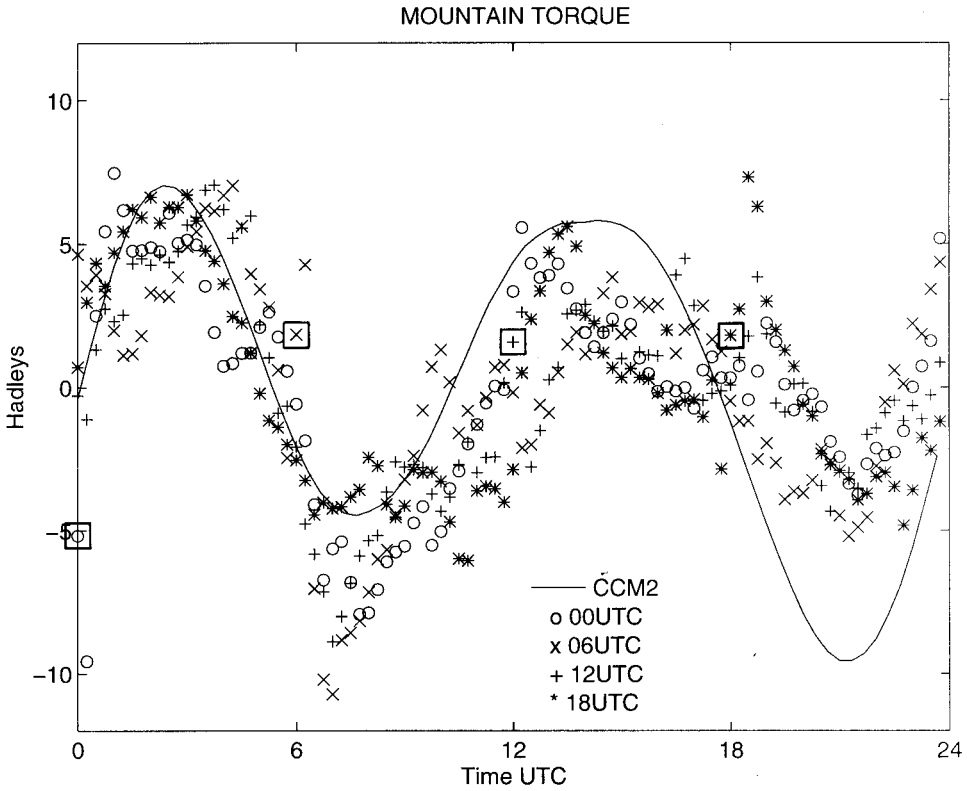

FIG. 13. The diurnal variation of T_m. The line is for CCM2 data and comes from Fig. 2. Other symbols represent the observations approximated by moving the four synoptic hour pressure maps around the earth past the mountains. Map values were shifted two grid points westward for each simulated time step. This results in 96 points, or simulated time steps, for each of the observed pressure anomaly maps. The "○" at 0000 UTC is the same as the asterisk at 0000 UTC in Fig. 2, and the "×" at 0600 UTC is the same as the asterisk at 0600 UTC in Fig. 2, etc. These four values from Fig. 2 are indicated by the squares.

NCEP/NCAR results being approximately out of phase on the semidiurnal timescale.

Of course, diurnal and semidiurnal change in M do not last for 24 h and actually make no change in LOD. A more meaningful variable is UT1 − TAI, which is the instantaneous difference between the time inferred from the rotation of the earth (UT1) and International Atomic Time (TAI). It is given by integrating Δ LOD since by definition

$$\frac{\Delta \mathrm{LOD}}{\mathrm{LOD}_0} = -\frac{d}{dt}(\mathrm{UT1} - \mathrm{TAI}) \tag{9}$$

(see, e.g., Gross 1993). Here LOD_0 is 86 400. The M_{eff} of Fig. 15 was Fourier analyzed and the amplitude of the diurnal and semidiurnal variations in terms of LOD from (7) and UT1 − TAI from the integral of (9) are presented in Table 2.

The out-of-phase relation of M_{eff} between model and NCEP/NCAR results rule out firm conclusions about phase. However, it seems safe to conclude from Table 2 that UT1 amplitudes driven by subdaily variations in M are the order of 1 μs or less, a conclusion consistent with Herring and Dong (1994), who found that they were likely on the order of 1 μs. This is a small fraction of the tens of microsecond amplitudes actually observed for UT1 and therefore also consistent with earlier demonstrations that it is tidal ocean angular momentum changes that are primarily responsible for subdaily variations in UT1 (e.g., Lichten et al. 1992; Herring and Dong 1994; Ray et al. 1994; Chao et al. 1995; Gipson 1996).

6. Summary

The NCAR Community Climate Model (CCM2) exhibits rather large diurnal and semidiurnal variations in its angular momentum budget. NCEP/NCAR Reanalysis data allow us to look for similar variations in the real atmosphere. There are clear semidiurnal variations in relative angular momentum and in omega momentum consistent with those suggested by the model data. The semidiurnal variation in M_Ω with maxima at 0600 and 1800 UTC reflect meridional mass exchanges and/or changes in water vapor loading with maximum mass near the equator at those hours (Fig. 12). In a current study, based on a simulation of the CCM3, we hope to be able to identify which process is most important. Interestingly, although M_r and M_Ω each have sizable

Unauthenticated | Downloaded 10/03/24 04:33 PM UTC

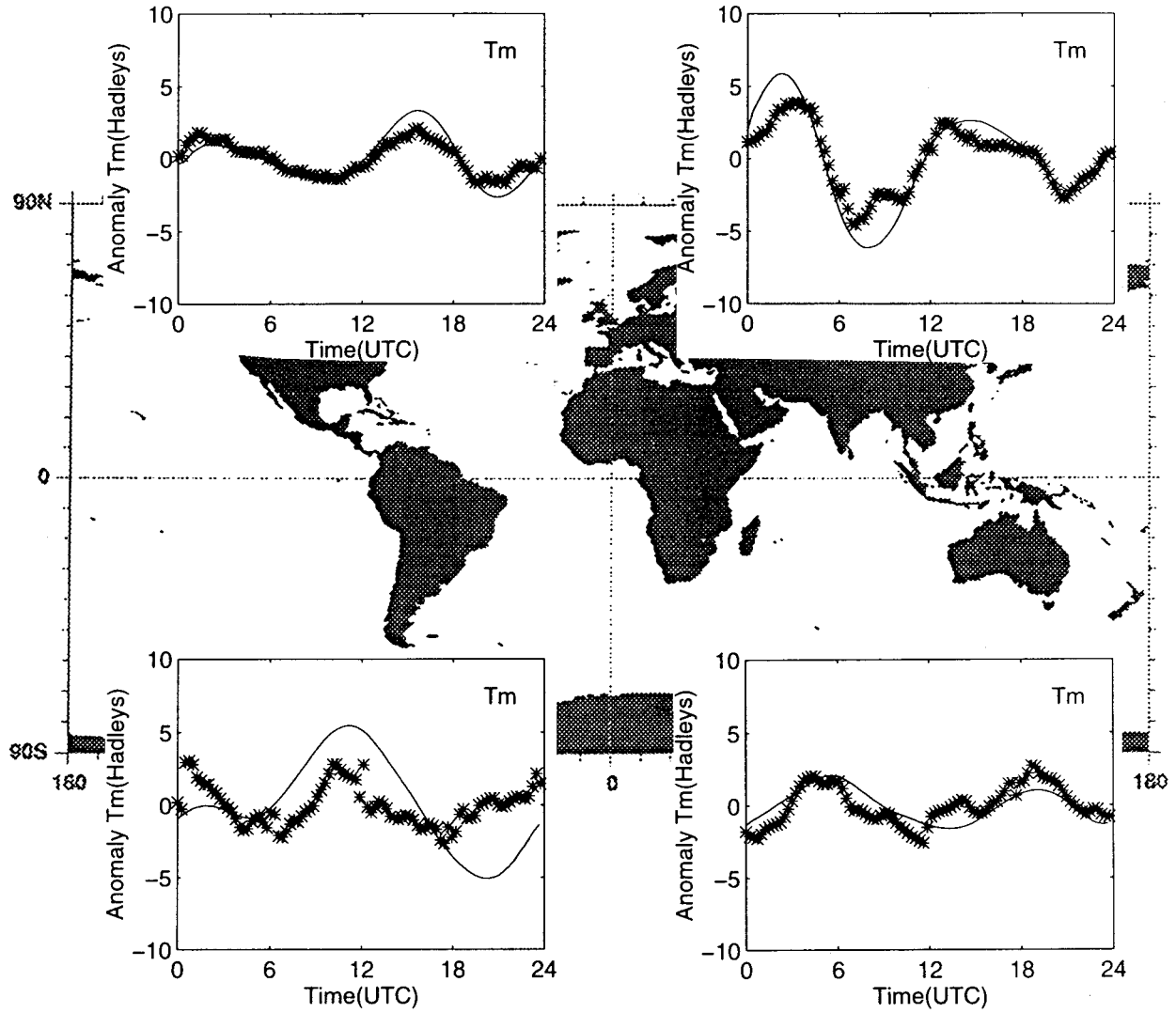

FIG. 14. Same as in Fig. 7 but with observed areal contributions simulated for 96 time steps during the day in a manner similar to that of Fig. 13 depicted by the asterisks. Rather than plotting values determined from each of the four anomaly pressure maps, for clarity, the asterisks are the average of the four. As a result values at the four synoptic times do not exactly match those in Fig. 7.

semidiurnal oscillations, because they are out of phase, their sum has a relatively small one.

Diurnal and semidiurnal variations in torques drive the variations in M. Most of the global variation in frictional torques comes from land areas where diurnally changing stability plays an important role in regulating the wind stress. The African continent is especially important. Nearly all the diurnal variation in gravity-wave drag torque comes from the Himalayas and mountains westward to the Black Sea. Again we suspect diurnal variations in stability and in surface winds to be the cause. There is reasonably good agreement between model variations and those reflected in four per day available observations. However, determining frictional and gravity wave stress from the NCEP/NCAR Reanalyses is model dependent and more study is needed to establish the truth and detail of their diurnal variations.

We believe that the most important contribution of this paper is documenting the semidiurnal variation in mountain torques that is caused by the migrating semidiurnal pressure wave. This pressure wave is well docu-

TABLE 2. Diurnal and semidiurnal amplitudes in UT1 − TAI (in μs) suggested by M_{eff} of Fig. 15. The LOD column comes from (7) and is the amplitude of LOD changes if ΔM lasted for 24 h. The UT1 − TAI column is from the integral of (9). Amplitudes for NCEP/NCAR are based on only four resolved values per day.

	Diurnal		Semidiurnal	
	LOD	UT1 − TAI	LOD	UT1 − TAI
Model	3.66	0.58	1.04	0.08
NCEP/NCAR	4.54	0.72	3.86	0.31

Unauthenticated | Downloaded 10/03/24 04:33 PM UTC

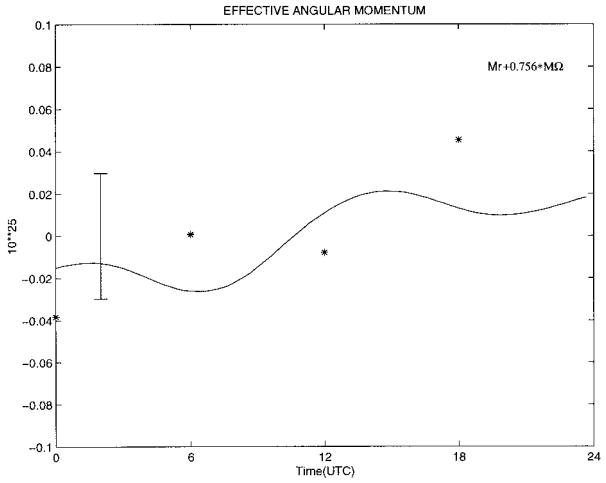

FIG. 15. Like the lower right panel of Fig. 2 with the ''effective'' M anomalies equal to $M_r + 0.756M_\Omega$. Units are 10^{25} kg m^2 s^{-1}. The vertical bar at the left represents a change in the effective M that, if it persisted for 24 h, would result in change of 10 μs in LOD.

mented in both models and observations. We show here that it produces peak-to-trough variations in mountain torques exceeding 10 Hadleys.

Consistent with earlier work, our results indicate that subdaily changes in M are only small contributors to similar changes in the earth's rotation rate. Finally, it should be noted that earth rotation is described by a three-dimensional vector. Only the axial component has been considered here. We plan to do a similar study of atmospheric variables that contribute to changes in the other two components associated with polar motion.

Acknowledgments. D. Holmstrom, D. Joseph, and Chi-Fan Shih helped us to access the reanalysis data. G. White provided information about the reanalysis methods. E. C. Rothney skillfully and patiently typed several versions of the manuscript. B. F. Chao carefully reviewed the paper, and he and an anonymous reviewer pointed out some errors in our first submission. D. Salstein, K. Hamilton, M. Hagan, and B. Boville helped us to understand several aspects of the problem.

REFERENCES

Barnes, R. T. H., R. Hide, A. A. White, and C. A. Wilson, 1983: Atmospheric angular momentum fluctuations, length-of-day changes and polar motion. *Proc. Roy. Soc. London*, **387A,** 31–73.

Chao, B. F., R. D. Ray, and G. D. Egbert, 1995: Diurnal/semidiurnal oceanic tidal angular momentum: TOPEX/Poseidon models in comparison with Earth's rotation rate. *Geophys. Res. Lett.,* **22,** 1993–1996.

Chapman, S., and R. S. Lindzen, 1970: *Atmospheric Tides.* Gordon and Breach, 200 pp.

Freedman, A. P., R. Ibañez-Meier, T. A. Herring, S. M. Lichten, and J. O. Dickey, 1994: Subdaily earth rotation during the E Poch '92 campaign. *Geophys. Res. Lett.*, **21,** 769–772.

Gipson, J. M., 1996: Very long baseline interferometry determination of neglected tidal terms in high-frequency Earth orientation variation. *J. Geophys. Res.*, **101,** 28 051–28 064.

Gross, R. S., 1993: The effect of ocean tides on the earth's rotation as predicted by the results of an ocean tide model. *Geophys. Res. Lett.,* **20,** 293–296.

Hack, J. J., B. A. Boville, B. F. Briegleb, J. T. Kiehl, P. J. Rasch, and D. L. Williamson, 1993: Description of the NCAR Community Climate Model (CCM2). NCAR Tech. Note NCAR/TN-382+STR, 108 pp. [Available from the National Center for Atmospheric Research, Boulder, CO 80307.]

Haurwitz, B., 1956: The geographic distribution of the solar semidiurnal pressure oscillation. Meteor. Paper, No. 2, New York University, 36 pp.

——, and A. D. Cowley, 1973: The diurnal and semidiurnal barometric oscillations, global distribution and annual variation. *Pure Appl. Geophys.,* **102,** 193–222.

Herring, T. A., and D. Dong, 1994: Measurement of diurnal and semidiurnal rotation variations and tidal parameters of earth. *J. Geophys. Res.,* **99,** 18 051–18 071.

Hsu, H.-H., and B. J. Hoskins, 1989: Tidal fluctuations as seen in ECMWF data. *Quart. J. Roy. Meteor. Soc.,* **115,** 247–264.

Kalnay, E., and Coauthors, 1996: The NCEP/NCAR 40-year Reanalysis Project. *Bull. Amer. Meteor. Soc.,* **77,** 437–471.

Lejenäs, H., R. A. Madden, and J. J. Hack, 1997: Global atmospheric angular momentum and earth–atmosphere exchange of angular momentum simulated in a general circulation model. *J. Geophys. Res.,* **102,** 1931–1941.

Lichten, S. M., S. L. Marcus, and J. D. Dickey, 1992: Sub-daily resolution of earth rotation variations with global positioning system measurement. *Geophys. Res. Lett.,* **19,** 537–540.

Lieberman, R. S., C. B. Leovy, B. A. Boville, and B. P. Briegleb, 1994: Diurnal heating and cloudiness in the NCAR Community Climate Model (CCM2). *J. Climate,* **7,** 869–889.

McFarlane, N. A., 1987: The effect of orographically excited wave drag on the general circulation of the lower stratosphere and troposphere. *J. Atmos. Sci.,* **44,** 1775–1800.

Munk, W. H., and G. J. F. MacDonald, 1960: *The Rotation of the Earth.* Cambridge University Press, 232 pp.

Newton, C. W., 1971: Global angular momentum balance: Earth torques and atmospheric fluxes. *J. Atmos. Sci.,* **28,** 1329–1341.

Ray, R. D., D. J. Steinburg, B. F. Chao, and D. E. Cartwright, 1994: Diurnal and semidiurnal variations in the earth's rotation rate induced by oceanic tides. *Science,* **264,** 830–832.

Rosen, R. D., 1993: The axial momentum balance of earth and its fluid envelope. *Survey Geophys.,* **14,** 1–29.

——, and D. A. Salstein, 1983: Variations in atmospheric angular momentum on global and regional scales and the length of the day. *J. Geophys. Res.,* **88,** 5451–5470.

Van den Dool, H. M., S. Saha, J. Schemm, and J. Huang, 1997: A temporal interpolation method to obtain hourly atmospheric surface pressure tides in reanalysis 1979–95. *J. Geophys. Res.,* **102,** 22 013–22 024.

Wahr, J. M., and A. H. Oort, 1984: Frictional- and mountain-torque estimates from global atmospheric data. *J. Atmos. Sci.,* **41,** 190–204.

Wallace, J. M., and R. F. Tadd, 1974: Some further results concerning the vertical structure of atmospheric tidal motions within the lowest 30 kilometers. *Mon. Wea. Rev.,* **102,** 795–803.

Whiteman, C. D., and X. Bian, 1996: Solar semidiurnal tides in the troposphere: Detection by radar profilers. *Bull. Amer. Meteor. Soc.,* **77,** 529–542.

Zwiers, F., and K. Hamilton, 1986: Simulation of solar tides in the Canadian Climate Centre General Circulation Model. *J. Geophys. Res.,* **91,** 11 877–11 896.

Unauthenticated | Downloaded 10/03/24 04:33 PM UTC